ELSEVIER

Welding: insights from high-temperature analogue experiments

Steven L. Quane, J.K. Russell[*]

Igneous Petrology Laboratory, Earth and Ocean Sciences, University of British Columbia, Vancouver, British Columbia,
Canada V6T 1Z4

Abstract

The rheological behavior of pyroclastic deposits during welding is incompletely understood and is based on a surprisingly small number of experimental studies. Here we present results from a new experimental apparatus comprising an automated uniaxial compression load frame that can run constant load (up to 1150 kg) or constant displacement rate (10^{-6} to 0.25 cm/s) tests at elevated temperatures (≤ 1100 °C). Deformation experiments were performed on pre-fabricated cylinders (4.5 cm diameter, ~6 cm length) of soda lime silica glass beads ($N=32$), sintered rhyolite ash ($N=7$) and cores of pumiceous rhyodacite ($N=6$). Experimental runs used strain rates from 10^{-5} to 10^{-3} s^{-1} and stresses of ~0 to 5.24 MPa. Temperatures varied from 535 to 650 °C for experiments on soda lime silica glass beads and 825 to 950 °C for natural materials. In all cases experimental cores showed a strain-dependent rheology that is more strongly affected by temperature than by load or strain rate. Results from these experiments are used to develop a relationship in which the effective viscosity (η_e) of the experimental cores is predicted by:

$$\eta_e = \eta_o \exp^{-5.3\left(\frac{\phi_f}{1-\phi_f}\right)}$$

where η_0 is melt viscosity and ϕ_f is sample porosity. This rheological model provides a means for exploring the relative roles of emplacement temperature, load and glass transition temperature in welding of pyroclastic deposits.
© 2004 Elsevier B.V. All rights reserved.

Keywords: welding; pyroclastic; experimental; strain; viscosity

1. Introduction

Welding of pyroclastic deposits involves flattening of glassy pyroclasts under a compactional load at temperatures above the glass transition temperature (T_g; e.g., Smith, 1960a; Ross and Smith, 1961; Ragan

* Corresponding author. Tel.: +1 604 822 2703; fax: +1 604 822 6088.
   E-mail address: krussell@eos.ubc.ca (J.K. Russell).

and Sheridan, 1972). Progressive welding is attended by pronounced changes in the physical character of the deposits (e.g., porosity loss, density increase, increased foliation; Smith, 1960a,b; Peterson, 1979; Streck and Grunder, 1995; Quane and Russell, 2004). The factors governing the intensity of welding in a pyroclastic deposit ultimately involve emplacement temperature, glass rheology, load pressure, particle size and distributions, as well as, the amount of time the deposit is held at temperatures $>T_g$ (e.g., Smith, 1960a; Guest, 1967; Riehle, 1973).

Welding in pyroclastic deposits is a process where laboratory experimentation can match the natural conditions (e.g., temperature, load pressure, time scale). Experiments on natural ash-lapilli-crystal mixtures, for example, can provide direct estimates of the minimum temperatures required for welding (e.g., Boyd, 1961; Friedman et al., 1963; Bierwirth, 1982). However, the complexities of the natural materials (e.g., grain size distributions, crystal content, glass composition) can obscure the fundamental aspects of welding. Our approach is to use both analogue and simple natural materials to explore the mechanisms and rheology of welding processes in pyroclastic rocks. Specifically, we have performed a series of high-temperature deformation experiments at both constant load and constant strain rate on sintered cores of soda lime silica glass beads. The experimental data from our experiments on homogenous analogue materials are used to establish a constitutive relationship between melt viscosity, porosity and effective viscosity of the material being welded that can later be applied to more heterogenous natural pyroclastic deposits. This constitutive relationship is applied, in conjunction with preliminary experiments on natural materials, to constrain the timescales of welding in pyroclastic deposits.

2. Previous experimental studies

Previous experimental studies of welding in pyroclastic deposits fall into two main categories (Table 1). Several were designed to establish a minimum temperature of welding (Boyd and Kennedy, 1951; Taneda, 1957; Boyd, 1961; Yagi, 1966; Akelaitis, 1999; Mossing, 2003; Grunder et al., 2005—this issue). Studies of Smith et al. (1958), Friedman et al. (1963) and Bierwirth (1982) also investigated the rates of welding deformation.

Boyd and Kennedy (1951) were the first to experimentally investigate welding in natural materials. They showed that dry rhyolite ash from Mono Craters, California welded at temperatures between

Table 1
Summary of experimental styles and conditions used to explore the welding of natural pyroclastic materials

Source	Material	Dimension $w \times h$ (mm)	N[a]	T (°C)	σ (MPa)	P_{H_2O}[b] (MPa)	dL/dt[c] (cm s^{-1})	Duration (h)	T_W[d] (°C)
Taneda (1957)	rhyolite pumice	*	*	600–1200	0.1–0.5	D	U	1.0–1.5	920
Boyd (1961)	rhyolite ash	2×4	12	550–755	2.8–5.2	D	U	72–430	590–620
Friedman et al. (1963); Smith et al. (1958)	rhyolite ash and pyrex glass	5×10	27	400–850	1.5–3.6	0–6.9	U	10–1000	635
Yagi (1966)	ash (rhyolite and andesite)	3×15	23	580–622	none	0.3–2	U	16–45	585
Bierwirth (1982)	ash (rhyolite and dacite)	9×22	*	650–800	0.72–3.6	D	U	17–70	650
Akelaitis (1999)	rhyodacite	100×150	*	600–1100	0.003	D	U	24	900
Mossing (2003)	rhyodacite pumice	20×30	7	850–950	0.25–4.86	D	10^{-4} to 10^{-5}	<1–5	850
Grunder et al. (2005—this issue)	rhyolite ash	4×10	35	600–1200	1–20	H	U	1–817	600
This study	glass beads	45×70	33	535–650	0–2.5	D	10^{-4} to 10^{-3}	<1–5	535

*Information not available.
[a] Number of experiments performed in study.
[b] Fluid pressure used in confined experiments which reduces the total effective load. Unconfined experiments were reported as dry (D, ambient atmosphere) or hydrous (H, saturated starting materials).
[c] Experimental displacement rates (U denotes uncontrolled).
[d] Minimum temperature at which welding features were observed.

775 and 900 °C depending on load pressures. Boyd (1961) expanded the study to include experiments on rhyolite ash (95 wt% ash, 5% crystals) containing 0–0.4% H_2O. Small samples were sealed in platinum capsules and placed in cold seal bombs under a fixed pressure (argon). He showed that the extent and minimum temperature of welding were strongly affected by the water content of the glass, confining pressure, and the experimental dwell time. Boyd (1961) concluded that the minimum temperature of welding for the Yellowstone tuff is on the order of 600 °C. The study includes a single photomicrograph of the experimentally welded ash and Boyd (1961) noted that the sample lacked the common traits associated with welding in pyroclastic material (e.g., eutaxitic alignment and deformation of bubble and Y-shaped ash shards). This "negative" result was ascribed to the fine-grained nature of the sample (no bubble-rich or Y-shaped shards) and the presence of a hydrostatic pressure. Nevertheless, these studies clearly demonstrate the effects of water content and confining pressure on welding processes.

Taneda (1957) varied temperature and load pressure in unconfined experiments to produce welded material. He used these results to make stratigraphic correlations between unwelded and welded facies of the same ignimbrite but also constrained welding conditions to below 920 °C at 0.5 MPa load pressure (~30 m depth). Smith (1960a) suggested that the minimum welding temperatures could be even lower because Taneda's (1957) samples would have been fully dehydrated at the temperatures used in the experiments. In a similar set of constant load experiments, Akelaitis (1999) showed that dry rhyodacite material deformed at average strain rates of 4×10^{-7}, 1×10^{-6} and 3×10^{-6} s^{-1} at temperatures of 800, 900 and 1000 °C, respectively, under a stress of 0.003 MPa.

Yagi (1966) explored the influence of melt composition on welding efficiency by working with three different materials. The compositions ranged from rhyolite (Shiritaki obsidian and Toya pumice) to andesite (Usu pumice). The samples were crushed and sieved to <0.2 mm and sealed in silver tubes with 10–20 cm^3 of H_2O and heated. Again, the hydrostatic pressure in the experimental runs prevented the development of compactional textures typical of natural welded tuffs. The study did, however, show

the compositional dependence of welding. At a temperature of 622 °C (under water-saturated conditions) the more siliceous Shiritaki obsidian was welded whereas the andesitic Usu pumice fall failed to weld.

Smith et al. (1958) and Friedman et al. (1963) aimed to constrain the actual rates and paths of welding. Friedman et al. (1963) used a deformation apparatus capable of constant load experiments at variable T and fluid pressure (Fig. 1a). Experiments were performed on samples of unwelded ash from the
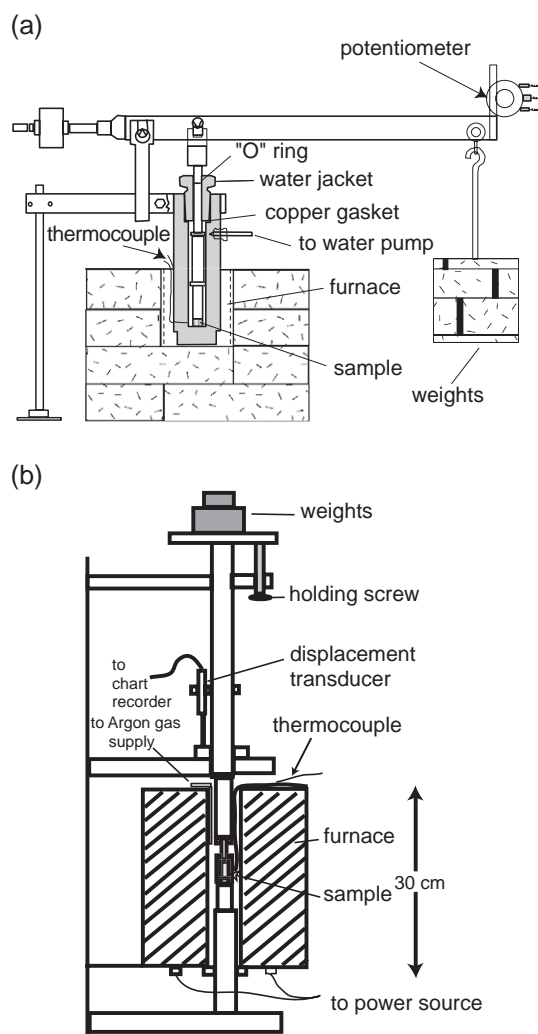
Fig. 1. Apparatus used in previous experimental studies of welding: (a) Friedman et al. (1963), (b) Bierwirth (1982). See text for discussion.

Bandelier Tuff having an initial porosity of ~50%. Material was shaken and compacted to ~1 cm thickness in a stainless-steel-jacketed copper vessel with a platinum liner and cover. A series of pistons were seated on top of the sample. The bomb was sealed with a cooled rubber O-ring and, to load the sample, weights were placed on a lever connected to the steel piston. Fluid (H_2O) pressure in the bomb was controlled with a hand pump. Displacement (e.g., compaction or shortening) was measured as a function of time by a potentiometer and recorded on a strip chart (Fig. 1a). The samples were confined laterally and, therefore, all shortening was assumed to be due to porosity loss. Thus, Friedman et al. (1963) was the first to produce data that could be analyzed in terms of porosity reduction with time. Experiments were run at temperatures between 485 and 900 °C and at load pressures up to 3.6 MPa: an equivalent thickness of ignimbrite of ~120 m. These data have been the basis for a number of computational models for simulating compaction and welding of pyroclastic material (e.g., Riehle, 1973; Riehle et al., 1995). There were no photomicrographs of the experimental run products, so the mechanisms of deformation in the experiments were not directly investigated.

Bierwirth (1982) also investigated the rates of compaction on ash from the Bandelier Tuff using a constant load apparatus (Fig. 1b). The starting material (71% ash and 29% crystals and lithics by weight) was sieved for the ash fraction (<2 mm) and packed into a small copper vessel to a thickness of 1 cm (Fig. 1b). Starting porosities were ~50%. The vessel was fitted on top with a copper disc and placed into a metal holder. A metal plunger was joined to a steel piston by a heat resistant alumina rod designed so that it had free travel into the sample vessel (Fig. 1b). Samples were flooded with argon during the experiment to prevent oxidation of the glass. Weights were placed on top of the piston assembly to deliver a specified load. Load was imposed instantaneously by release of a retaining screw (Fig. 1b). A displacement transducer connected to the central piston measured shortening as a function of time (Fig. 1b) and strain was assumed to represent porosity loss. Bierwirth (1982) showed several photomicrographs of the resulting ash mixture. These experiments produced a range of textures that are normally associated with progressive welding facies (e.g., bubble and Y-shaped

shard deformation). Furthermore, deformed pumice lapilli have flattening ratios up to ~7 which is consistent with observations made on densely welded natural samples (e.g., Ragan and Sheridan, 1972; Quane and Russell, 2004).

The experiments of Friedman et al. (1963) and Bierwirth (1982) used the same material; however, they produced different results. For example, under conditions of atmospheric confining pressure and no H_2O pressure a sample deformed by Friedman et al. (1963) at 635 °C under a load pressure of 3.63 MPa showed complete loss of porosity in ~16 h. Bierwirth (1982) experimented under a similar load (2.89 MPa) and at a higher temperature (650 °C) but produced virtually no porosity loss over the same dwell time. The different results can be attributed to different experimental techniques. Specifically, the sample vessel of Bierwirth (1982) is not sealed, thus, pore pressure is always equal to atmospheric pressure and, upon heating the sample, H_2O escapes from the glass, raising its effective viscosity. Conversely, the Friedman et al. (1963) vessel was sealed and the glass was able to retain its H_2O. Potentially, higher H_2O pressures would cause the glasses to absorb H_2O (Friedman et al., 1963; Bierwirth, 1982) thereby lowering its viscosity (e.g., Sparks et al., 1999). This would increase the potential for welding. However, it is unlikely all the water in these experiments was dissolved into the glass, in which case, the remaining H_2O pressure must provide pore fluid pressure that negates the effects of the compactional load. This issue needs to be addressed in future studies.

When combined, these pioneering studies elucidate the effects of composition, load and confining pressure on the nature and degree of welding in pyroclastic deposits. Furthermore, they provide minimum welding temperatures and a first look at the rates of welding for a variety of different environmental conditions. The relevance of each experimental dataset to natural welding processes is directly related to the experimental design. Realistically, it is impossible to replicate all conditions in nature; however, the more advanced the device (e.g., Friedman et al., 1963; Bierwirth, 1982) the more relevant the data is to the natural process. The data produced from these studies (Table 1) are neither sufficiently comprehensive nor coherent enough to fully describe the rheology of pyroclastic mixtures.

In addition, the small sample sizes used in these studies do not allow for a full examination of the microstructural and geometric changes associated with welding compaction. Inspired by these studies, we have designed an apparatus capable of running controlled deformation experiments on large samples at elevated temperatures.

3. Experimental device

The base unit of the Volcanology Deformation Rig (VDR; Fig. 2) is a LoadTrac II® loadframe manufactured by Geocomp. Specifics on the device and its calibration can be found in Quane et al. (2004). The unit performs both constant displacement rate and constant load tests. Displacement speed ranges from 5×10^{-6} to 2.5×10^{-2} cm s^{-1} and a built-in LVDT displacement transducer measures
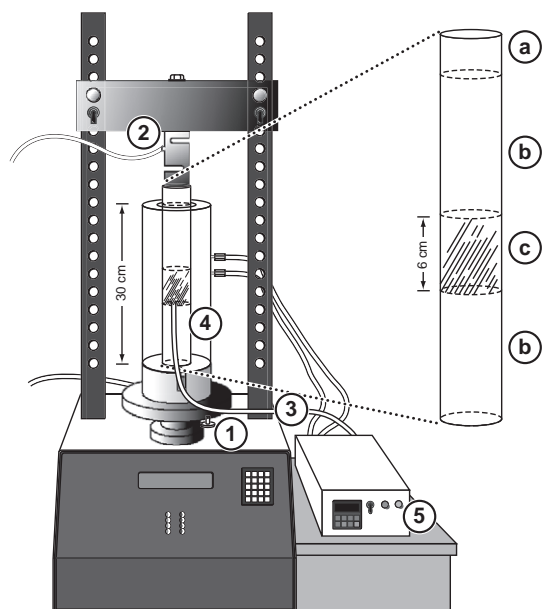
Fig. 2. Schematic representation of the Volcanology Deformation Rig (VDR) used in this study. Unit comprises a Geocomp® Corporation Load Trac II load frame with (1) LVDT displacement transducer, and (2) load cell having a 1136 kg limit. Modifications made to the load frame for use at high temperatures include: (3) thermocouple, (4) fiber insulated furnace, and (5) temperature controller. The sample assembly is attached to the load cell and comprises a steel spacer (a) and two high temperature ceramic pistons (b) located above and below the sample (c).

displacement during the experiment (7.6 cm travel range and 0.00013 cm resolution). Samples can be loaded at rates from zero to 1.9 kg/s and the maximum attainable load is 1136 kg with 86 g resolution. Experimental output (i.e., measurements) can be collected every 0.01 s throughout the experiment.

The VDR accommodates cylindrical samples having maximum diameters and lengths of 4.95 cm and 10 cm, respectively (Fig. 2). The experiments in this study are performed on non-jacketed cores of coherent material (e.g., pumice cores) however, the VDR can be used to experiment on unconsolidated materials (e.g., volcanic ash). The piston and sample assembly have been constructed to facilitate high-T experiments (e.g., >500 °C; Fig. 2) on large samples (e.g., 750 cm^3). Our measurements show a symmetric temperature profile that reaches steady-state after a 1 hour dwell time, and shows a total variation of ~12 °C (Quane et al., 2004).

The VDR is designed to explore a range of experimental parameters that is unique within the rock deformation community (Fig. 3a). Many volcanic processes, including welding, are characterized by conditions of low stress (Fig. 3b) and conventional triaxial rock presses have poor resolution at such low loads (e.g., Handin et al., 1972; Austin, 2003; Fig. 3a). Furthermore, welding occurs at strain rates substantially slower than those explored during decompression experiments (e.g., Spieler et al., 2003; Mangan et al., 2003; Fig. 3a and b). The VDR allows for isothermal experiments under the conditions of constant displacement rate or constant load. Each experiment generates a nearly continuous high-resolution set of raw measurements including: time (s), load (kg), and displacement (cm) from which we compute stress (MPa) and strain. Stress (σ) is calculated from:

$$\sigma = \text{load}/\left(\pi r^2\right) \qquad (1)$$

where r is the radius of the sample core. Although the load cell has an upper limit of 1136 kg, this relationship between core geometry and stress can be exploited to extend the upper and lower ranges of the VDR. In natural systems, welding typically operates under stresses <5 MPa (Fig. 3b), however, the VDR can achieve stresses as high as ~150 MPa
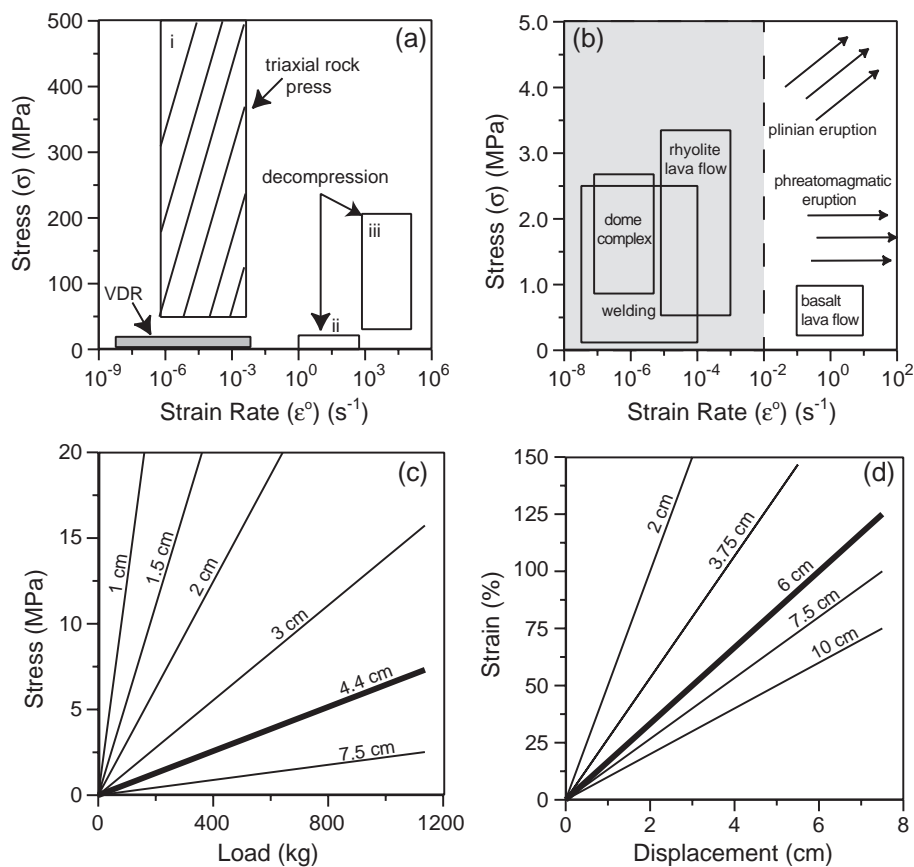
Fig. 3. Range of experimental parameter space available to VDR (shaded gray boxes) compared to: (a) stress–strain rates available to: (i) conventional triaxial rock press (e.g., Handin et al., 1972; Austin, 2003) (ii, iii) decompression experiments simulating fragmentation (Spieler et al., 2003) or vesiculation and fragmentation (Mangan et al., 2003), respectively. (b) Average stresses and strain rates attending common volcanic events. Stress for each event is calculated from load expected at the base of deposits. Strain rates are implied by average extrusion rates, flow rates or compaction rates depending on the process. Explosive events (phreatomagmatic and plinian eruptions) occur at a variety of stresses and strain rates which are higher than shown on this schematic. Lower panels show relationships between machine controlled parameters (load and displacement) and rheological variables stress and strain for the VDR. (c) Load (kg) vs. stress (MPa) relationships for different experimental core diameters used on the VDR. Maximum load of apparatus is 1136 kg. Thick line represents core diameter used in this study. (d) Displacement (cm) vs. strain (%) relationships for different core lengths. Maximum allowable displacement of the apparatus is 7.5 cm. Thick line represents approximate core length used in this study.

by using 1 cm diameter cores (Fig. 3c). We principally use 4.5 cm diameter cores because they provide abundant material for post-experiment analysis.

The VDR allows a total displacement of 7.6 cm which means that a range of core lengths can be used for relatively high strain experiments (Fig. 3d). Our experiments use ~6 cm length cores. Strain (ε) is calculated as:

$$\varepsilon = \Delta l / l_c \qquad (2)$$

where Δl is the experimental displacement and l_c is the original length of the sample. The core length is corrected for pre-deformational shortening which occurs over the heating (30 min) and equilibration dwell time (60 min) that precedes each experiment. At temperatures $>T_g$ the glass can deform under its own weight causing changes in l_c and the sample porosity. A linear calibration was used to correct for this pre-experiment deformation by quenching the experiments without deformation and re-measuring the core length and porosity. The corrections

are 0, 1.35, 4.5, and 9% for temperatures of 535, 550, 600 and 650 °C, respectively. This shortening is accommodated exclusively by porosity loss (i.e., no core radius change). After applying this temperature-dependent correction, displacements are converted to strain.

4. Analogue experimental material

Analogue materials provide a vehicle for simplifying experimental models. For example, they are used in experiments that simulate lava flow dynamics (e.g., waxes; Fink and Griffiths, 1990; Griffiths, 2000; Soule and Cashman, 2003), caldera collapse processes (e.g., sand rubber bladders and silicone; e.g., Roche et al., 2000; Acocella et al., 2003; Lavallee et al., 2004) or fragmentation of magma (e.g., Hill and Sturtevant, 1990; Mader et al., 1994; Phillips et al., 1995; Mourtada-Bonnefoi and Mader, 2003). Here, we use soda lime silica glass beads as an analogue material for exploring

the mechanisms and timescales of welding in pyroclastic deposits. The glass beads have several important attributes. First, the individual beads have known physical properties. This allows us to use the density of the glass (2.49 g/cm^3) as a known for calculating porosity (ϕ) in our pre-and post-run products from:

$$\phi = \frac{\rho_{\mathrm{m}} - \rho_{\mathrm{T}}}{\rho_{\mathrm{m}}} \qquad (3)$$

where ρ_{m} is the matrix (bead) density and ρ_{T} is the bulk density of the sample. Second, the beads are spherical in shape having a maximum variation in sphericity of ±10%. Hence, where deformed under known conditions, each individual bead acts as a strain marker. Third, soda lime silica glass has a uniform composition (Table 2) and a relatively low glass transition temperature (T_{g}=~490–550 °C). This allows deformation experiments to be run at lower temperatures (e.g., <600 °C). We have calculated the viscosity of the soda lime glass beads as a function of temperature (Lakatos, 1976; Fig. 4a; Table 2) from

Table 2

Composition of soda-lime silica beads used in experiments and values of viscosity computed from model Vogel-Tammann-Fulcher equation predicted after Lakatos (1976)[a]

Oxide	Wt.%	T (°C)	$10000/T$ (K)	$\log \eta$ (Pa s)
SiO$_2$	66	450	13.83	21.76
Al$_2$O$_3$	5	500	12.93	15.79
ZnO	2	550	12.15	12.2
MgO	1	600	11.45	9.79
CaO	7	650	10.83	8.07
Na$_2$O	15	700	10.28	6.78
K$_2$O	1	750	9.77	5.77
B$_2$O$_2$	3	800	9.32	4.97
Sum	100	850	8.90	4.31
		900	8.52	3.76
		950	8.18	3.29
		1000	7.85	2.89
		1050	7.56	2.54
		1100	7.28	2.24
		1150	7.03	1.97
		1200	6.79	1.74

		$\log \eta$ (Nom)	$\log \eta$ (Calc)	Δ
T-softening 735 °C	$\log \eta$-softening	6.6	6.1	0.5
T-annealing 548 °C	$\log \eta$-annealing	12.2	12.3	−0.1

Also reported are nominal and model values of viscosity at the annealing and softening temperatures.

[a] $\log \eta$ (poise)=−1.32+3654/[T(°C)−298].
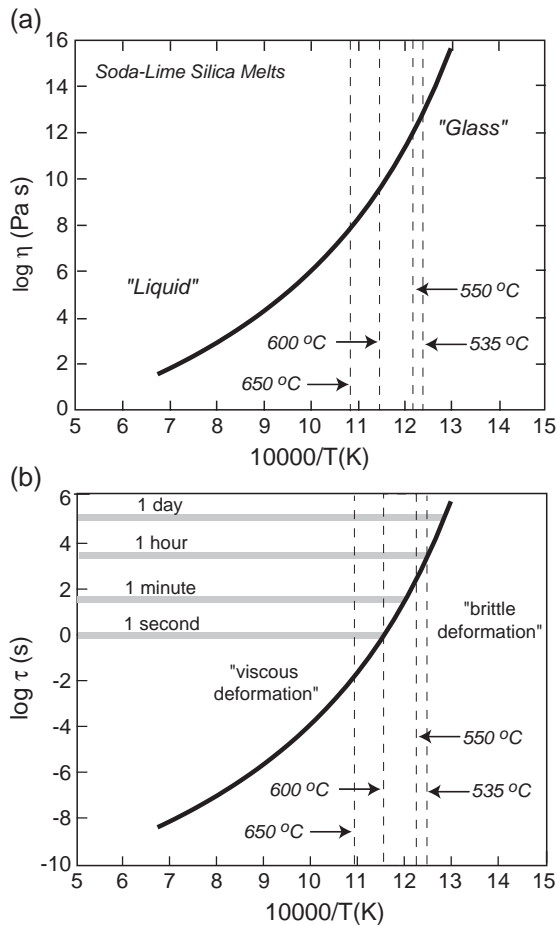
Fig. 4. (a) Viscosity (Pa s)–temperature (K) relationship for soda lime silica glass. Vogel-Tammann-Fulcher fit equation (Table 2) is calculated from nominal composition using procedure of Lakatos (1976). (b) Relaxation timescale (τ)–temperature relationship for soda lime silica glass determined using the Maxwell relationship (Dingwell and Webb, 1990). Vertical dashed lines represent experimental temperatures from this study. Gray horizontal bars show characteristic relaxation timescales used to select experimental temperatures.

which we calculate the characteristic relaxation timescales (τ) for the soda lime silica liquid:

$$\tau = \eta/G_\infty \qquad (4)$$

where η is the viscosity of the liquid and G_∞ is the bulk shear modulus of silicate melts ($10^{10\pm0.5}$ Pa; Maxwell, 1867; Burcaro and Dardy, 1974; Bansal and Doremus, 1986; Dingwell and Webb, 1990). The characteristic relaxation timescales of the soda lime glass liquid range from 1 s to ~1 h over the temperature interval used in this

study (Fig. 4b). At a given temperature the experimental deformation rate must be slower than the relaxation timescale to support viscous deformation.

Our experiments were performed on cores of sintered 1 or 2 mm soda lime beads. The cores were fabricated using an 8 cm long stainless steel cylinder that was split lengthwise. The inner surface of the steel cylinder was coated with molycote® and dry flake graphite lubricant to avoid the glass wetting the steel and the cylinder was filled with beads to a height of 6–7 cm. The halves of the cylinder were fastened by stainless steel hose clamps and the beads were capped by a ceramic spacer (4 cm diameter; 2 cm length) to provide a flat upper surface to the core. The sample was held at 600 °C for 75 min and then cooled to room temperature over 12 h to avoid thermal cracking of the glass. The core was removed, washed and dried for 24 h at ~100 °C. Resulting cores (Fig. 5) have a diameter of 4.5 cm and lengths of ~6 cm. Porosity of the starting material ranges from ~30 to 36% (Table 3) compared
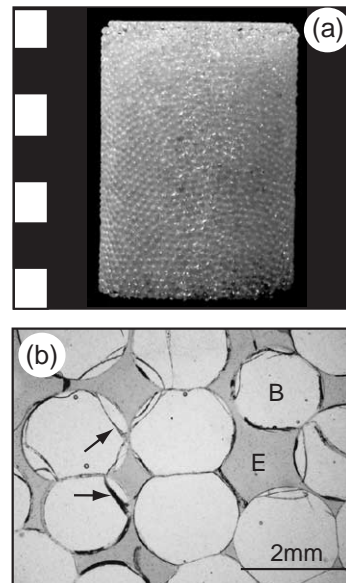
Fig. 5. Representative starting material used in this experimental study. (a) Right circular cylinder comprising sintered 2 mm soda lime silica glass beads. Porosities of starting materials range from ~30 to 36%. Method used to fabricate cores is described in text. (b) Thin section photomicrograph of the same core after impregnation with dyed epoxy (E). The individual beads (B) remain essentially undeformed during sintering. Cracks in individual glass beads (see arrows) result from thin section preparation.

Table 3
Summary of conditions of high-temperature deformation experiments performed on cores of soda lime beads and properties of run products[a]

No. (sq-)	T (°C)	dL/dt (cm/s)	σ (MPa)	ΔL	ε_T	ϕ_0	ϕ_f	r_f	ε_a	ε_r	Ob	η_e (Pa s)
06_24a	600	2.5e−04	*	4.000	0.59	0.346	0.097	2.85	0.28	0.38	0.64	1.12e+09
06_24b	600	1.0e−03	*	4.575	0.59	0.324	0.037	3.19	0.28	0.50	0.75	2.45e+09
06_25a	600	5.0e−04	*	3.920	0.60	0.327	0.089	2.92	0.26	0.41	0.65	1.30e+09
06_25b	550	5.0e−04	*	3.800	0.60	0.378	0.226	3.09	0.22	0.47	0.53	2.40e+10
06_27a	600	5.0e−04	*	4.550	0.62	0.308	0.049	3.13	0.27	0.48	0.72	2.15e+09
07_04a	600	5.0e−04	*	4.200	0.60	0.306	0.064	3.00	0.26	0.44	0.70	1.53e+09
07_04b	600	2.5e−04	*	4.085	0.60	0.303	0.053	2.98	0.26	0.43	0.72	1.72e+09
07_16a	650	5.0e−04	*	4.075	0.50	0.274	0.037	2.89	0.25	0.39	0.73	3.76e+08
07_16b	550	5.0e−04	*	3.520	0.50	0.351	0.140	2.85	0.25	0.38	0.48	1.10e+10
07_17a	600	5.0e−04	*	2.625	0.34	0.298	0.124	2.54	0.20	0.22	0.45	3.21e+08
07_17b	600	1.0e−03	*	3.910	0.50	0.340	0.089	2.81	0.28	0.36	0.65	9.61e+08
07_18a	600	*	0.060	3.050	0.40	0.294	0.128	2.70	0.19	0.30	0.58	5.43e+08
07_18b	600	*	0.050	2.900	0.35	0.313	0.152	2.60	0.19	0.25	0.50	3.66e+08
07_19a	600	*	0.045	2.000	0.30	0.297	0.158	2.48	0.17	0.18	0.42	2.18e+08
07_22a	600	*	0.037	1.800	0.25	0.320	0.194	2.34	0.16	0.08	0.37	1.23e+08
07_22b	600	*	0.031	1.630	0.20	0.323	0.193	2.37	0.16	0.10	0.32	1.45e+08
07_22c	600	*	0.024	1.200	0.15	0.319	0.297	2.27	0.03	0.02	0.24	1.46e+08
07_23a	600	*	0.026	0.900	0.10	0.329	0.307	2.25	0.03	0.00	0.18	7.94e+07
07_23b	600	*	0.033	3.100	0.34	0.365	0.167	2.51	0.24	0.20	0.49	4.43e+08
07_24a	600	5.0e−04	*	4.300	0.50	0.292	0.102	3.03	0.17	0.45	0.71	9.87e+08
07_24b	600	*	0.058	4.375	0.56	0.304	0.058	3.11	0.23	0.48	0.72	1.59e+09
07_28a	550	*	0.170	2.850	0.40	0.369	0.156	2.49	0.25	0.18	0.53	5.77e+09
08_04a	600	*	0.015	2.950	0.36	0.308	0.109	2.56	0.22	0.23	0.13	3.28e+08
08_06a	550	*	0.111	1.900	0.29	0.285	0.146	2.41	0.16	0.13	0.47	3.50e+09
08_06b	550	*	0.035	1.610	0.16	0.344	0.291	2.29	0.07	0.03	0.31	2.48e+09
08_07b	535	*	0.161	1.775	0.34	0.329	0.228	2.39	0.13	0.11	0.43	1.20e+10
08_08a	535	*	0.322	2.725	0.40	0.353	0.215	2.56	0.18	0.22	0.53	1.28e+10
08_08b	535	*	0.036	1.150	0.17	0.351	0.292	2.31	0.08	0.05	0.25	3.50e+09
08_09a	535	*	0.160	1.925	0.28	0.326	0.229	2.47	0.13	0.17	0.39	9.09e+09
08_11a	535	*	0.160	2.250	0.33	0.288	0.169	2.51	0.14	0.20	0.52	9.71e+09
08_11b	600	5.0e−04	*	3.600	0.50	0.274	0.097	2.79	0.20	0.35	0.65	5.41e+08
08_12a	600	5.0e−04	*	3.700	0.45	0.288	0.083	2.87	0.23	0.39	0.62	5.24e+08
08_04b	600	*	*		0.279	0.279	–	–	–	–	–	–

Experiments use constant displacement rate (dL/dt) or constant load (e.g., stress, σ).

[a] Parameters include: shortening (ΔL), total strain (ε_T), initial porosity (ϕ_0), final porosity (ϕ_f), final radius of core (r_f), axial (ε_a) and radial (ε_r) strain, oblateness (Ob), and effective viscosity (η_e).

with 36.3% which is the theoretical minimum porosity for random packing of solid spheres (Scott and Kilgour, 1969).

5. Experimental results

Our results derive from thirty-two experiments on sintered cores of soda lime silica glass beads performed under a constant displacement rate or constant load constraint (Table 3). Displacement rates varied from 2.5×10^{-4} to 1×10^{-3} cm/s; loads ranged from ~5 to 50 kg (σ=0.03 to ~0.35 MPa). Experiments were performed at constant temperatures of 535, 550, 600 and 650 °C on cores comprising 1 mm, 2 mm and a mixture of 1 and 2 mm beads. To a first order, there were no apparent differences in the rheology that could be attributed to grain size.

5.1. Constant displacement rate

Results are presented in Fig. 6 for constant displacement rate experiments at rates of 5×10^{-4} cm/s, 2.5×10^{-4} cm/s and 1×10^{-3} cm/s and temperatures of 550 and 600 °C. For a 6 cm length core these displacement rates translate into strain rates of
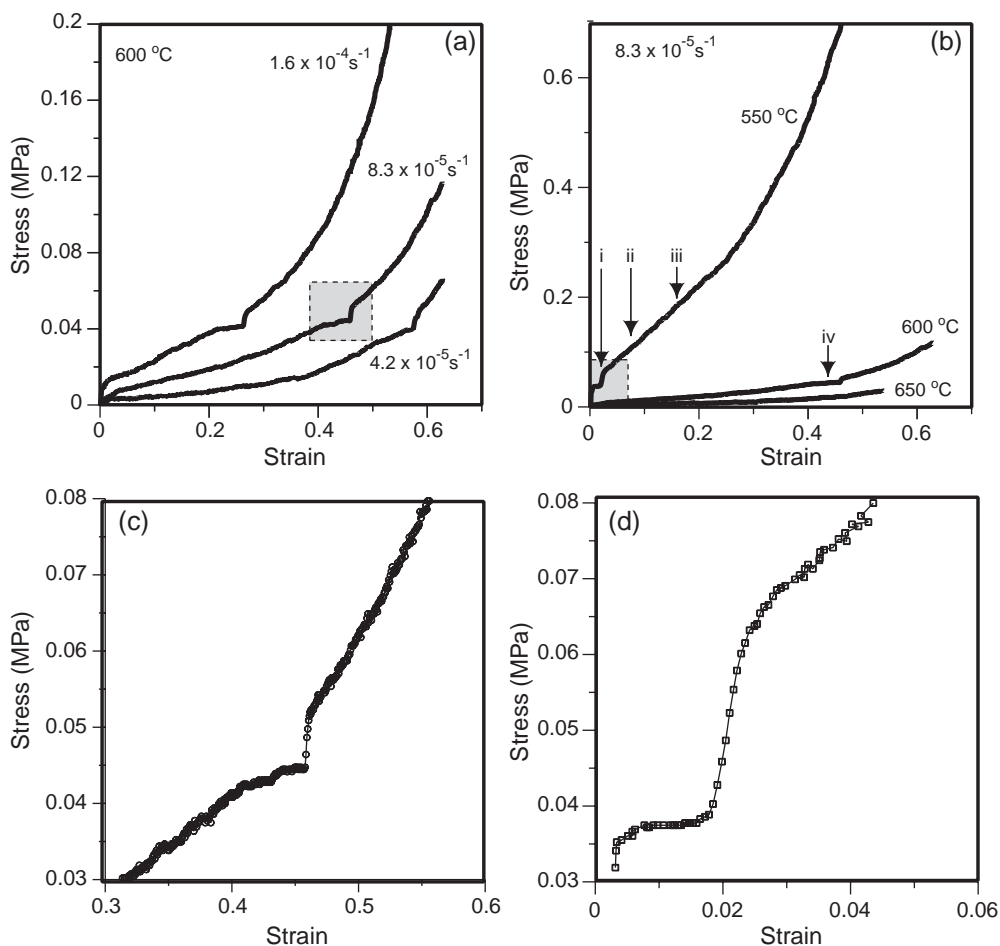
Fig. 6. Experimental results from constant displacement rate experiments on cores of glass beads. Data are plotted as stress (MPa) vs. strain: (a) 600 °C isothermal experiments performed at 3 different strain rates (see labels). Experimental output shows smooth non-linear increase in stress until ~0.04 MPa where the stress/strain ratio increases markedly. Shaded area is magnified in (c). (b) Constant displacement rate experiments illustrating the effect of temperature (550, 600, 650 °C) on rheological behavior of glass bead cores. The same step in stress–strain curves is seen at ~0.04 MPa. Shaded area is enlarged in (d).

4.16×10^{-5} s^{-1}, 8.3×10^{-5} s^{-1} and 1.6×10^{-4} s^{-1} respectively. These strain rates allow for 50% strain over timescales of 12,000 to 3000 s. In constant displacement rate experiments the bottom platen of the VDR moves upward at a specified rate resulting in a linear accumulation of strain with time. Increasing strain is accompanied by a relatively smooth non-linear accumulation of stress on the sample (Fig. 6) and is manifest in the cores by a loss of porosity and by flattening of individual beads perpendicular to the displacement direction (Fig. 7). Changing displacement rate has a noticeable effect

on the stress–strain relationship (Fig. 6a). Faster rates of displacement result in larger stresses at lower amounts of strain. Lowering temperature has a similar effect on the rheology; lower temperatures result in a more rapid accumulation of stress (Fig. 6b). Temperature has a much larger effect on rheology than displacement rate. A reduction in temperature from 600 to 550 °C (~10%) results in a ~10 times increase in stress at a strain of 0.2, whereas a 100% increase in displacement rate (5×10^{-4} to 1×10^{-3} cm/s; Fig. 6) results in only a ~2-fold increase in stress.
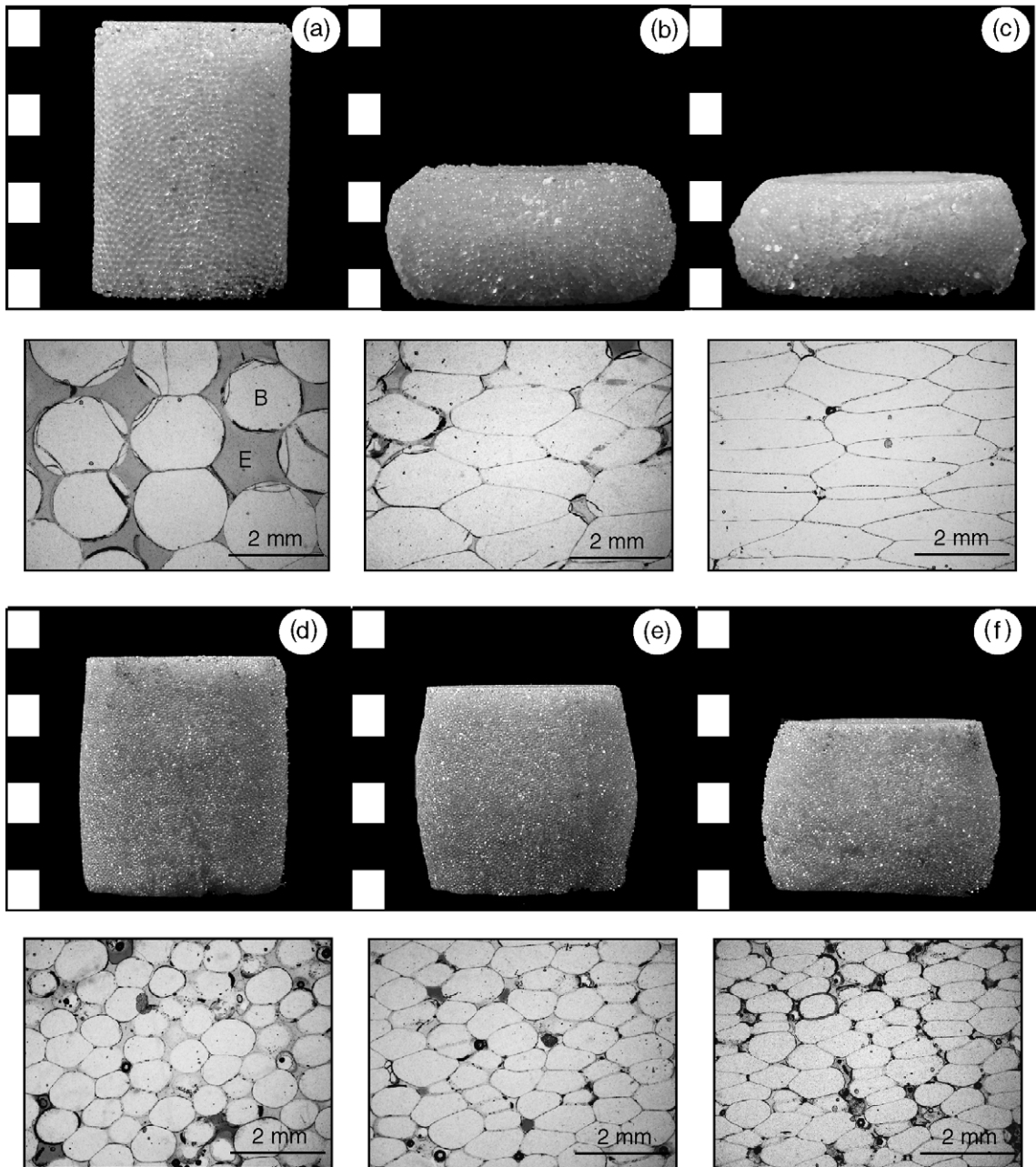
Fig. 7. Photographs and corresponding thin section photomicrographs for experimental end products observed in this study. (a) Representative starting material with an initial porosity of 31% (Table 3; sq-08_04b). Virtually undeformed glass beads (B) can be differentiated from colored epoxy (E) in thin section. (b) Run product from experiment sq-06_25b: 2 mm beads, 55.8% strain at a strain rate of 8.3×10^{-5} s^{-1} and final porosity of 20.5%. (c) Experiment sq-06_27a: 2 mm beads, 63.6% strain at a strain rate of 8.3×10^{-5} s^{-1} and final porosity of 5.3%. (d) Experiment sq-08_06b: 1 mm beads, 15.5% strain at a constant stress of 0.035 MPa and final porosity of 29%. (e) Experiment sq-08_06a: 1 mm beads, 28.9% strain at a constant stress of 0.11 MPa and final porosity of 14.6%. (f) Experiment sq-07_28a: 1 mm beads, 39.7% strain at a constant stress of 0.17 MPa and final porosity of 15.6%.

S.L. Quane, J.K. Russell / Journal of Volcanology and Geothermal Research 142 (2005) 67–87

Relatively smooth curvilinear stress–strain relationships are shown by 550 and 600 °C experiments up until a stress of ~0.04 MPa is reached (Fig. 6a and b). A stress of ~0.04 MPa seems to separate two different regimes. Below ~0.04 MPa increasing strain causes a smooth increase in stress. At ~0.04 MPa there is a discontinuous jump in stress after which the stress–strain curve steepens markedly. The position of this rheologic discontinuity, in terms of strain, is controlled by both displacement rate and temperature. At the same temperature, increasing displacement rate causes the discontinuity to shift to lower values of total strain (Fig. 6a). Again, temperature has a

stronger control than displacement rate on this process. At the same displacement rate lowering temperature causes the discontinuity to occur at much lower values of strain (Fig. 6a and b). When explored in detail the discontinuity has the same form; however, the lower temperature experiment shows a much higher jump in stress (Fig. 6c and d).

5.2. Constant load

Here, we present data from four experiments performed at constant loads of 5.2, 15.95 and 24.95 kg and temperatures of 550 and 600 °C. These loads
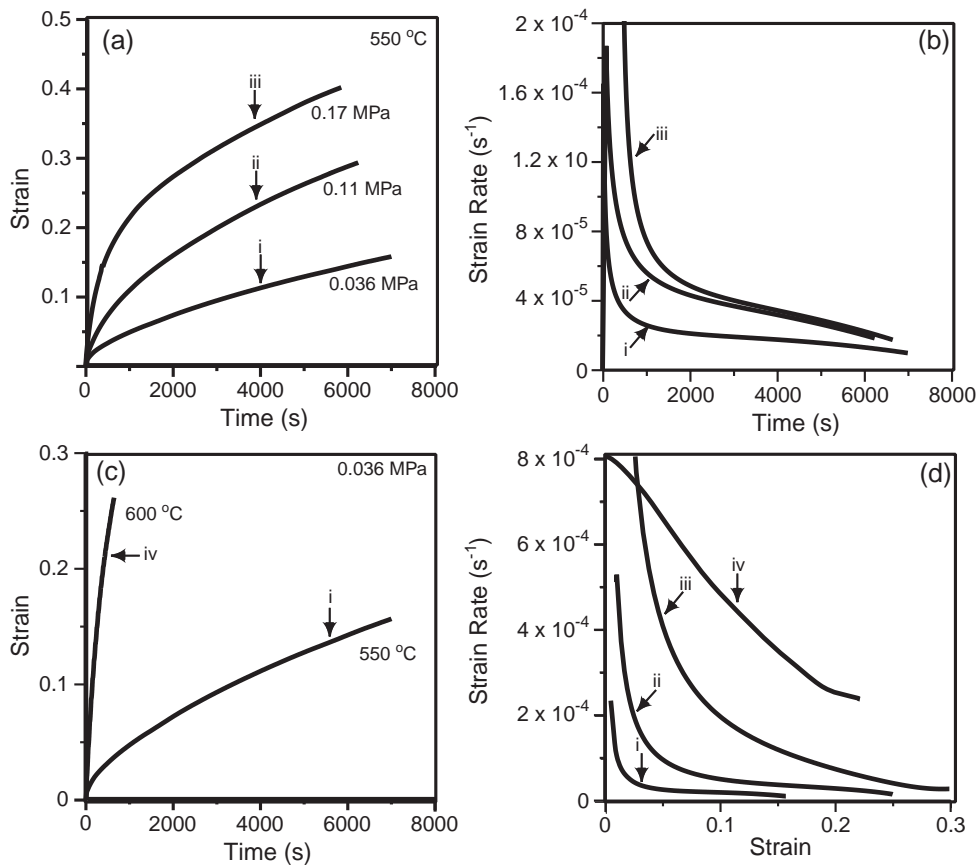
Fig. 8. Experimental results from constant stress experiments on cores of glass beads. (a) Strain vs. time plot for experiments on 1 mm beads at 550 °C and at different imposed stresses (i, ii, iii). Experimental stresses were chosen from the 550 °C rheological curve shown in Fig. 6b. Larger stresses result in greater amounts of strain for a given time. (b) Evolution of strain rate with time for experiments shown in (a). Higher stress experiments support higher strain rates but converge to a common value. (c) Effect of temperature on constant load deformation paths. Higher temperature experiment (iv; 600 °C) deforms much more rapidly than lower temperature (i, 550 °C) at the same imposed stress. (d) Strain rate vs. strain relationship for constant load experiments. The higher temperature sample (iv) remains at a much higher strain rate than the lower temperature samples (i, ii, iii).

were selected from different points on the stress–strain relationships illustrated in Fig. 6b (i–iv). For a 4.5 cm diameter core, these loads equal stresses of 0.036, 0.11 and 0.17 MPa, respectively and are roughly equivalent to depths of ~2, 6 and 10 m in a pyroclastic deposit.

In a constant load experiment, the bottom platen of the VDR is raised at a specified rate until the present load is reached. From this point onwards, the platen only moves upward in order to maintain the specified load. Strain increases in the sample non-linearly with time (Fig. 8). As strain accumulates, pore space is lost and individual beads become progressively more deformed (Fig. 7). We have calculated apparent strain rates from the derivatives of the curves fitted to the strain-time data sets (Fig. 8a,c). The strain rates are plotted against time in Fig. 8b and d. The strain rates and the ultimate strain achieved are dependent on the imposed stress and temperature (Fig. 8). Logically, higher loads (i.e., stress) result in higher initial strain rates and more total strain for a given amount of time (Fig. 8). As shown by constant displacement rate experiments, the rheology of the material is strongly temperature dependent. Decreasing the temperature from 600 to 550 °C (~10%) results in a 10 times reduction in accumulated strain at a time of 750 s (Fig. 8c). Conversely, a 300% increase in stress (0.036 MPa to 0.11 MPa) translates to a mere 3-fold increase in accumulated strain (Fig. 8a). These relationships have

important implications for the efficiency of welding processes in nature. For example, relatively thin deposits of pyroclastic material can achieve significant welding (e.g., Sparks and Wright, 1979) if they are emplaced at temperatures much greater than the material's T_g.

6. Data analysis

6.1. Mechanisms of strain

The above results describe the rheology of welding in an analogue system. To what extent can these results be applied to welding processes in natural systems (e.g., ignimbrites)? To address this issue, we present a preliminary set of experiments on cores of pumiceous rhyodacite (N=6) and sintered cores of rhyolite ash (N=7; Table 4). These data are used to compare how deformation is accommodated in cores of soda lime silica glass beads relative to natural volcanic materials.

Strain accumulation in the experimental cores is manifest in several ways, including: (a) reduction of core length (i.e., shortening), (b) change of core geometry (e.g., barreling), (c) reduction of primary porosity (i.e., volume loss), and (d) deformation of original spherical particles (e.g., flattening). These indicators of strain represent the combined effects of

Table 4
Summary of conditions used in experiments on natural materials (cores of ash and pumice) and properties of experimental run products[a]

No. (sq-)	T (°C)	dL/dt (cm/s)	σ (MPa)	ΔL	ε_T	ϕ_0	ϕ_f	r_f	ε_a	ε_r	η_e (Pa s)
08_19a	800	2.50e−04	*	1.85	0.36	0.81	0.75	2.34	0.23	0.15	4.86e+10
08_22a	835	2.50e−04	*	2.400	0.45	0.8	0.7	2.34	0.34	0.15	2.49e+10
08_23b	875	2.50e−04	*	2.685	0.48	0.8	0.67	2.3	0.40	0.12	1.86e+10
08_24a	850	1.25e−04	*	2.450	0.47	0.82	0.71	2.32	0.38	0.14	6.07e+10
08_25a	850	5.00e−04	*	2.590	0.49	0.8	0.66	2.31	0.41	0.13	3.65e+10
08_25b	850	5.00e−04	*	1.475	0.23	0.8	0.78	2.28	0.12	0.11	1.17e+10
08_26b	850	*	0.280	1.825	0.34	0.81	0.75	2.28	0.25	0.11	3.95e+10
mps_1	850	2.50e−04	*			0.700	0.285	1.23	0.58	0.23	*
mps_2	950	2.50e−04	*		0.76	0.722	0.277	1.41	0.62	0.41	*
mps_3	850	*	4.860		0.52	0.723	0.475	1.20	0.47	0.19	*
mps_5	950	*	1.650		0.65	0.750	0.344	1.16	0.62	0.14	*
mps_8	950	*	0.900		0.64	0.718	0.336	1.24	0.58	0.23	*
mps_9	950	*	5.240		0.79	0.754	0.375	1.52	0.61	0.50	*

Experiments use constant displacement rate (dL/dt) or constant load (e.g., stress, σ).

[a] Parameters include: shortening (ΔL), total strain (ε_T), initial porosity (ϕ_0), final porosity (ϕ_f), final radius of core (r_f), axial (ε_a) and radial (ε_r) strain, oblateness (Ob), and effective viscosity (η_e).

axial strain (ε_a) accommodated by porosity loss (volume strain) and radial strain (ε_r), which conserves volume and requires geometric changes (pure shear strain) (Fig. 9).

We measured the following physical properties for each experimental core: (a) initial porosity (ϕ_0), (b) final porosity (ϕ_f), (c) initial radius (r_0), (d) final radius (r_f) and (e) average oblateness of the individual beads in each core (Fig. 9; Table 3). Values of ϕ_0 derive from measurements of density (Eq. (3)) whereas ϕ_f is based on image analysis of thin sections (Table 3). Values of r_f and r_0 represent the average of ~10 caliper measurements taken at regular intervals along the length of the pre and post-experiment cores, respectively. We determined particle oblateness in each end product using:

$$1 - c/a \tag{5}$$

where c is the axial (height) and a the radial (length) dimension of each individual bead. To determine the axial and radial dimensions of individual beads we made an image of each thin section using a standard microfiche reader and hand traced bead outlines (~500 for 2 mm bead section and ~1000 for 1 mm bead sections). Traces were scanned and individual grains were fit to an ellipse using Scion® image analysis software. The fit provided values of c and a for each particle. The reported values for oblateness

(Table 3) are the mean of all traced beads in each section.

Average values for oblateness plot on the theoretical curvilinear relationship for pure shear strain (i.e., constant volume strain; Fig. 10a). This also shows all deformation in these experiments to be purely coaxial. However, because these experiments are not laterally confined, strain has two components; axial strain (ε_a) accommodated by porosity loss and radial strain (ε_r) accommodated by bulging of the sample. These components are calculated independently from:

$$\varepsilon_a = \frac{\phi_0 - \phi_f}{1 - \phi_f} \tag{6}$$

where ϕ_0 is the initial sample porosity and ϕ_f the porosity of the run product (Table 3) and from:

$$\varepsilon_r = 1 - \frac{r_0^2}{r_f^2} \tag{7}$$

where r_0 is the radius of the core before experiment and r_f the mean radius of the run product (Table 3). Calculated values of ε_a and ε_r are plotted in Fig. 10b. For experiments with moderate T (e.g., 600 °C) and deformation rate 5×10^{-4} cm/s there is a 1:1 relationship between ε_a and ε_r until ~40% total strain is attained (Fig. 10b). At this point porosity is reduced to ~10% and ε_r becomes dominant. The
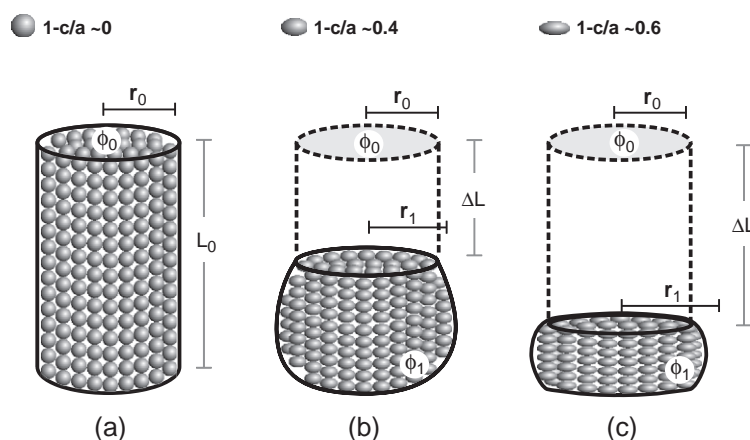
Fig. 9. Schematic illustration of mechanisms for accommodating strain during deformation experiments on glass bead cores. (a) Starting material having original porosity (ϕ_0), sample length (l_0) and core radius (r_0). Particles are essentially spherical. (b) and (c) Progressive deformation causes changes in porosity (ϕ_0 reduced to ϕ_f), length (Δl), particle shape (oblateness) and radius (bulging). Physical property measurements on experimental end products are used to determine the proportion of axial (ε_a) and radial (ε_r) strain for each sample (see text).
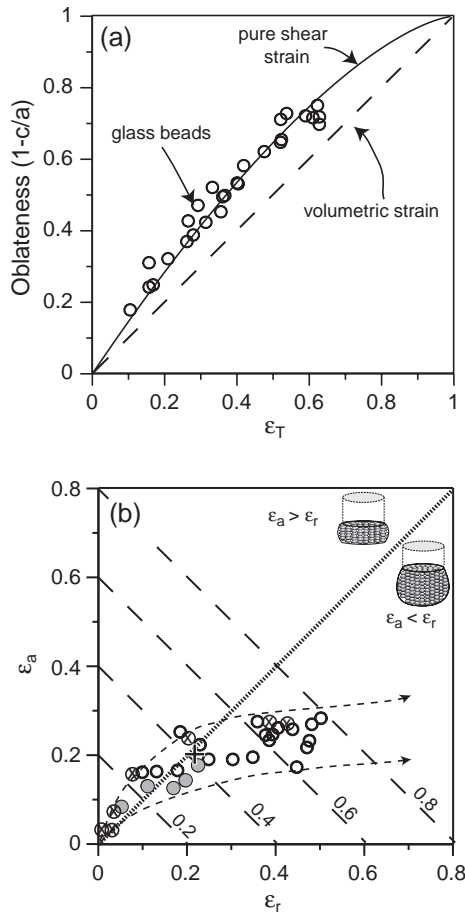
Fig. 10. Analysis of strain in high-T deformation experiments of cores of glass beads. (a) Comparison of average particle oblateness to total strain for each deformation experiment. Data plot on or near solid line which is the theoretical relationship between particle oblateness and strain for pure shear strain (constant volume). Dashed line is theoretical relationship for volumetric strain. (b) Comparison of axial strain (ε_a) and radial strain (ε_r) for experiments involving soda lime silica glass beads. Heavy dashed lines are iso-strain contours. Dotted line represents 1:1 relationship between ε_a and ε_r. Schematic in upper right corner shows the physical manifestation of the different types of strain accumulation. Experiments are coded for experimental conditions: low T and high strain rate (gray); high T, low σ or strain rate (circles with crosses) and intermediate (open circles). Radial strain is more dominant in deformation paths exhibited by the lower T and high strain rate experiments.

datum plotted as a cross (Fig. 10b) represents a constant displacement rate experiment (600 °C) that was stopped at the rheologic discontinuity shown in Fig. 6. Because this experiment plots essentially on

the 1:1 line, it appears that, up to the discontinuity, strain is accommodated equally through porosity loss (ε_a) and barreling (ε_r). This point demarcates the inception of ε_r as the dominant method of strain accommodation.

The paths for experiments under other conditions are different and appear to be controlled by T and strain rate. For example, in lower T experiments (gray circles; Fig. 10b) radial strain (ε_r) dominates the early portion of the deformation path. Conversely, higher T and lower strain rate experiments produce a path where ε_a is dominant (circles with X; Fig. 10b).

In natural systems, starting porosities can be higher (~50–75% e.g., Smith, 1960b; Ross and Smith, 1961; Smith and Bailey, 1966; Sheridan and Ragan, 1976) and include both matrix porosity and the porosity of the individual pyroclasts. As strain accumulates, clasts deform (flatten) but, in contrast to the glass beads, the deformation of the pyroclasts is not limited by a constant volume constraint (e.g., Sheridan and Ragan, 1976; Quane and Russell, 2004). The consequences of this difference are expressed in two ways. Firstly, values of oblateness from natural samples of the Bandelier Tuff (Quane and Russell, 2004), show that pumice lapilli, after being corrected for original oblateness, deform solely by volumetric strain. This contrasts with the behavior of the glass bead cores which demonstrate pure shear strain (e.g., constant volume; Fig. 11a). Secondly, in natural materials ε_a (e.g., volume strain) dominates over ε_r until very high values (~80%) of total strain. At this point, presumably all pore space has been lost and, thus, further strain is dominantly radial (ε_r; Fig. 11b). Regardless of these differences, our analysis strongly suggests that, in analogue and especially in high-porosity natural materials, porosity distributions ultimately control the mechanisms and extent of welding.

6.2. Strain dependent rheology

Results from both constant displacement rate and constant load experiments indicate that the glass bead mixtures have a strain dependent rheology. In Fig. 12a, we plot experimental data from 600 °C experiments at three different strain rates (x-axis). The results are plotted as stress (observed variable)
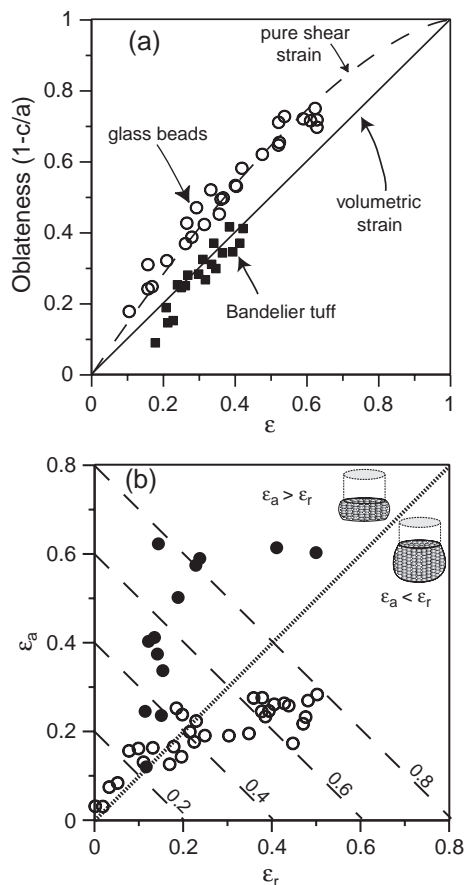
Fig. 11. Analysis of strain in high-T deformation experiments of cores of glass beads, pumice, and volcanic ash. (a) Comparison of average particle oblateness to total strain for experiments on soda lime silica glass beads (open circles) and naturally deformed pumice lapilli (black diamonds) from the Bandelier Tuff (Quane and Russell, 2004). Natural materials plot on the straight-line relationship representing volumetric strain (ϕ loss). Natural pyroclasts lose porosity during deformation unlike the solid glass beads used in this study. (b) Comparison of axial strain (ε_a) and radial strain (ε_r) for experiments involving soda lime silica glass beads (open circles) and natural pumice and ash (solid circles). ε_a is dominant in natural materials up to ~0.8 total strain. This relationship is due to the high inherent porosity of natural pyroclasts.

of strain is somewhat dependent on strain rate at low values of strain, whereas at higher strains the rheology is independent of strain rate (i.e., linear
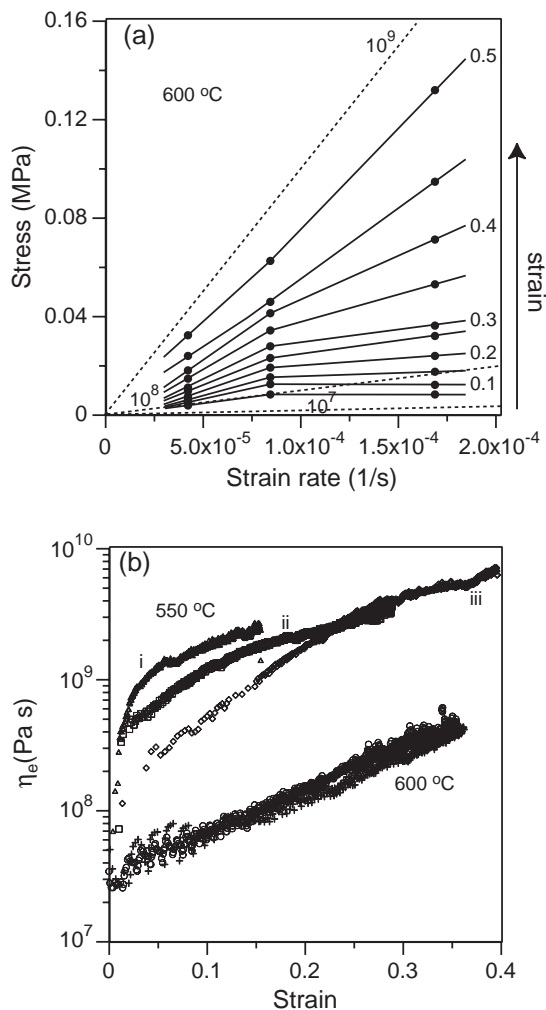
Fig. 12. Summary of constant displacement and constant load experiments on cores of glass beads. (a) Experimental stress is plotted against imposed strain rate for fixed increments of strain. Solid lines are for equal strain and the slope of the lines equal the effective Newtonian viscosity. Differences between lines show how rheological properties evolve with increasing strain. Dotted lines denote fixed viscosities of 10^7, 10^8 and 10^9 Pa s. (b) Results of constant load experiments are summarized as calculated effective viscosity (η_e) vs. strain for five experiments at two temperatures: (i) 550 °C, 0.035 MPa (triangles), (ii) 550 °C, 0.11 MPa (squares) and (iii) 550 °C, 0.17 MPa (diamonds) are the same as in Fig. 6. Data from 600 °C experiments include stresses of 0.05 MPa (crosses) and 0.033 MPa (circles). Values of η_e increase linearly (600 °C) and non-linearly (550 °C) with strain.

and strain rate (fixed experimental condition) for equal increments of strain (e.g., 0.05–0.5). The ratio of stress to strain rate defines the effective viscosity (η_e) of the cores during deformation. The data in Fig. 9a clearly show that as strain increases the implied value of η_e (slope) changes drastically (from ~10^7 to ~10^9 Pas). The η_e at a fixed amount

trend). The upper limit to this is reached where porosity goes to zero and the glass bead core approaches the viscosity of the soda lime glass ($10^{9.79}$ Pa s at 600 °C).

For the constant load experiments we have calculated η_e at each time step using the expression:

$$\eta_e = \frac{\sigma}{\overset{\circ}{\varepsilon}_i}. \tag{8}$$

The instantaneous strain rate ($\overset{\circ}{\varepsilon}_i$) for each time step in the experiment is calculated from:

$$\overset{\circ}{\varepsilon}_i = \frac{\Delta\varepsilon}{\Delta t} \tag{9}$$

where $\Delta\varepsilon$ is the incremental increase in strain for each time step and Δt is the duration of each time step (s). These data are plotted in Fig. 12b and show how η_e increases with increasing strain. For example, the 600 °C experiments show a moderate and steady increase in η_e with strain. Similarly, the 550 °C datasets show a strong, rapid increase in η_e with increasing strain. Together, the 550 and 600 °C datasets show that η_e and its rate of change are controlled by temperature. The magnitude of stress can also affect the rheological evolution of the samples. For the 550 °C experiments, increasing load delays the increase in η_e relative to lower load deformation paths.

During the deformation experiments strain is partially accommodated in the cores by porosity loss (e.g., Fig. 7), which causes changes in the η_e (e.g, Ducamp and Raj, 1989; Sura and Panda, 1990). The relationship between η_e (Eq. (8)) and porosity (ϕ) is explored by plotting ϕ vs. η_e (Fig 13a). Experimental data are grouped by temperature and fitted to:

$$\log_{10}\eta_e = \log_{10}\eta_0 - \alpha\left(\frac{\phi_f}{1-\phi_f}\right) \tag{10}$$

where α is an adjustable parameter, η_e is the observed value of viscosity at ϕ_f (Table 3) and η_0 is the viscosity of the melt at zero porosity. We have fit all of the experimental data to Eq. (10) simultaneously to derive model values for the viscosity (η_0) of the soda lime silica melt at each experimental temperature and a common α. There is good agreement between the expected values of η_0
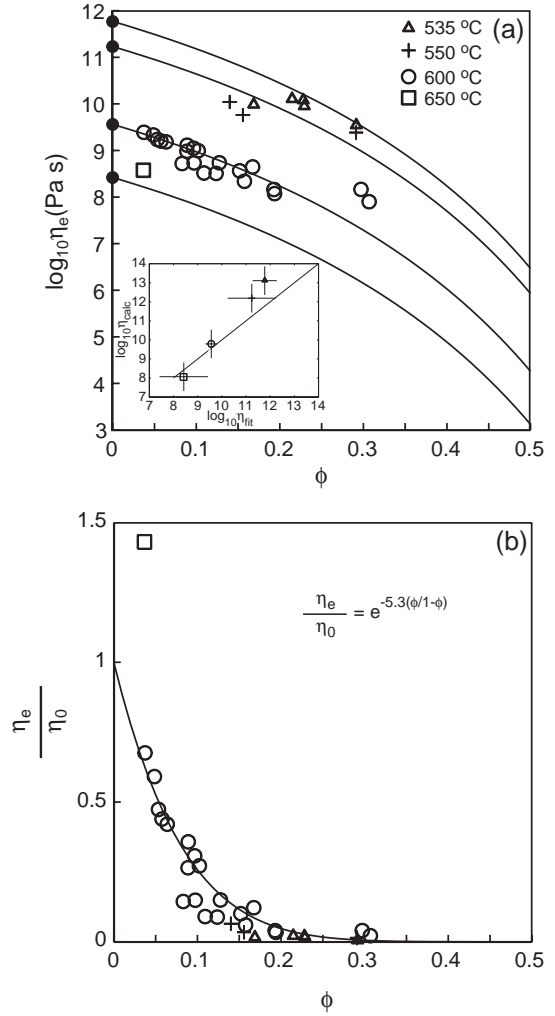
Fig. 13. Summary of porosity–viscosity relationship for experimental results on soda lime beads. (a) Porosity vs. log η data for each experimental temperature 650 °C (squares), 600 °C (circles), 550 °C (crosses) and 535 °C (triangles) show the increase in η_e as porosity decreases. Fitted curves (Eq. (10)) for each set of experiments have a Y-intercept value that defines the viscosity of soda lime silicate liquid (η_0) at the experimental T. Inset shows agreement between calculated values of η_0 (Lakatos, 1976; Table 2) and the values of η_0 derived from fitting these experimental data. (b) The viscosity of the mixture η_e is normalized by η_0 and plotted against ϕ. The data have an exponential relationship described by the equation in upper right hand corner.

(e.g., Lakatos, 1976; Table 2) and the values derived from fitting data from these deformation experiments (Fig. 13a). Our fit to the experimental data (Fig. 13b) returns a value for α of 5.3 and allows for the

prediction of η_e as a function of porosity (ϕ_f) and melt viscosity (η_0):

$$\frac{\eta_e}{\eta_0} = \exp^{-5.3\left(\frac{\phi_1}{1-\phi_f}\right)} \qquad (11)$$

A similar relationship using α values between 2.4 and 4.0 was found for experiments run on dry glass powder (Ducamp and Raj, 1989). This relationship is a first step in developing a constitutive relationship for welding in pyroclastic deposits comprising the parameters σ, ε, strain rate and ϕ.

7. Implications for welding

Within a sheet of pyroclastic material, stress increases linearly with depth due to lithostatic loading (Fig. 14a). Furthermore, each position in a pyroclastic deposit has a characteristic residence time in the welding interval (i.e., $T > T_g$) that can be predicted by simple conductive cooling models (e.g., Riehle, 1973; Miller, 1990; Russell and Quane, 2005—this issue). The top and base cool quickly (i.e., short residence times) whereas the interior of the deposit is insulated and has substantially longer residence times (e.g.,

Riehle, 1973; Miller, 1990; Russell and Quane, 2005— this issue; Fig. 14b). We represent these times for each sample using D_t^* which is calculated by normalizing the time a specific sample has within welding interval to the maximum time seen by any sample. The data from constant load deformation experiments run at 535 °C (Fig. 14c) are used to represent samples at 2.2, 10 and 20 m depth in a 20-m-thick pyroclastic deposit (Fig. 14a). The experimental data are plotted in Fig. 14c; each sample describes a unique deformation path (i.e., strain accumulation with time). Conceptually, each sample is arrested along its potential deformation path when it cools and passes out of its welding window ($t > D_t^*$; Fig. 14c) by being "quenched" at the T_g isotherm. The resulting strain in each sample (Fig. 14d) is a product of both the load (stress) and time of residence within the welding window. The deformation paths can be very different for each sample. For example, samples associated with large D_t^* values (e.g., middle of deposit) can undergo significant strain under lower loads (Fig. 14d). Conversely, samples with low values of D_t^* require high strain rates to attain equivalent strain. By way of example, the sample at 20 m depth accumulates more strain than an equivalent sample at 2.2 m depth even though it reaches the T_g isotherm sooner. Clearly, in this case, the higher load
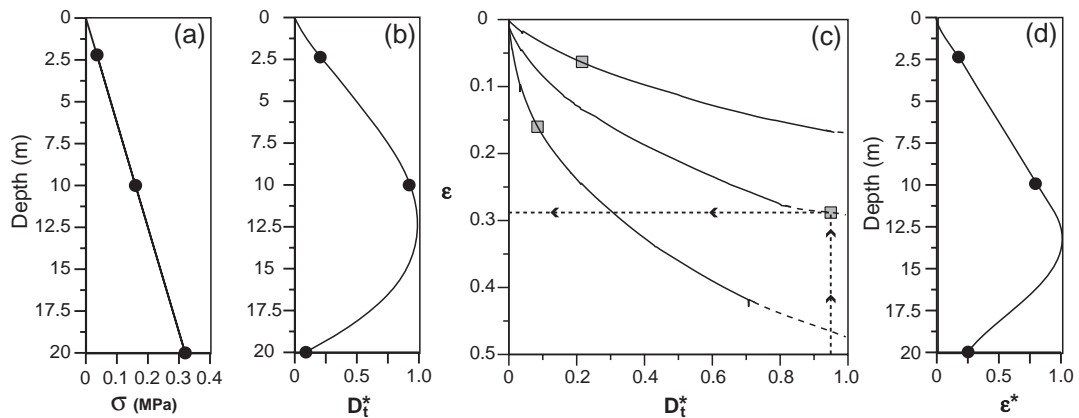
Fig. 14. Application of experimental data to strain accumulation in a single cooling unit of pyroclastic material. (a) Relationship between depth (m) and stress (MPa) for a 20-m-thick unit of pyroclastic material. Samples used in this figures are located at 2.2, 10 and 20 m depth. (b) Relative residence time (D_t^*) as a function of depth for a 20-m-thick unit cooling conductively. D_t^* is equal to the time that each sample resides above the minimum temperature of welding divided by the maximum time experienced by any sample. (c) Deformation paths for the three samples as a function of relative residence time. Gray boxes represent the intersection of the cooling curves (b) with the deformation path generated by the load each sample is subjected to. Total accumulated strain is determined by Y-intercept value for each intersection. (d) Normalized strain (ε^*; strain in each individual sample divided by maximum strain in deposit) accumulated in (c) as a function of depth.

provides higher strain rates and compensates for the shorter D_t* (Fig. 14d).

Not all pyroclastic deposits follow this simple model for cooling and strain accumulation. For example, thin pyroclastic deposits have been observed to undergo significant welding (e.g., Sparks and Wright, 1979). Such thin packages of pyroclastic material feature low loads and cool relatively quickly (e.g., Riehle, 1973; Miller, 1990) thereby shortening potential time of residence in the welding interval. However, our constant load experiments show that, even at low values of imposed stress, if $T >> T_g$ the resulting strain rate can be surprisingly high. Samples lost >50% of their porosity over a timescale of thousands of seconds (Fig. 8c). Therefore, under conditions of high emplacement temperatures (relative to T_g) even thin packages (low σ) of pyroclastic material can undergo significant welding. This reflects the fact that, where emplacement temperatures are greatly in excess of T_g, the relaxation timescale of the melt can be very short (e.g., Dingwell and Webb, 1990). The consequence is that significant amounts of strain can accumulate in a relatively short amount of time (e.g., Fig. 8c).

The majority of our analysis is based on results from experiments on analogue materials. These cores of glass beads are useful in describing the strain dependent rheology of porous aggregates during porosity loss. However, like all experiments on analogue materials, the ones performed in this study have limitations when applied to natural processes. For example, the analogue materials comprise solid spheres of glass of a uniform grain size (e.g., 1 mm, 2 mm or mixture of 1 and 2 mm). The cores essentially represent perfectly sorted materials. With few exceptions (e.g., medial fall deposits), natural pyroclastic deposits typically comprise poorly sorted mixtures of angular, porous pyroclasts including both pumice lapilli (>10 mm) and fine (<0.1 mm) ash particles. The internal porosity, angularity and random distribution of natural pyroclasts would likely lead to a substantially different rheology and, thus, require a different value for α (e.g., Fig. 13; Eqs. (10) and (11)). In addition, the heterogeneities in natural deposits would probably favor strain localization during welding where pumice could deform more intensely than the ash matrix (e.g., Sheridan and Ragan, 1976; Streck and Grunder, 1995; Quane and Russell, 2004).

The effects of H_2O on the welding process are also not explored by this experimental study. Firstly, the analogue materials do not contain any measurable H_2O whereas natural glasses can contain substantial amounts of dissolved H_2O. The dissolved H_2O strongly controls the viscosity of the glass and can potentially exsolve during high-temperature deformation. The latter effect could lead to pore fluid pressures that would retard welding and compaction. Conversely, the presence of excess H_2O in the system has the potential to become resorbed into the glass (e.g., Sparks et al., 1999), lower the viscosity and promote welding. In summary, the experiments on analogue materials provide key insights into the rheology of pyroclastic materials during welding, however, many potential avenues for further experimental study remain open.

8. Conclusions

We have explored the viability of soda lime silica glass beads as an analogue material for welding deformation in pyroclastic deposits. The predictable viscosity–temperature relationship, relatively low glass transition temperature and regular geometry of the glass bead analogue materials facilitate study of the rheology of glassy porous mixtures. Our results showed that temperature has a much stronger influence on the rheology of these materials than load or strain rate. The implication is that the difference between emplacement temperature and glass transition temperature ($T_e - T_g$) is the most important variable in welding. Secondly, under natural conditions, volume strain by porosity loss dominates during welding except under extraordinary conditions. These conditions might be met in situations where emplacement temperatures are extremely high or materials are deposited on a significant slope (e.g., Wolff and Wright, 1981). Lastly, the rheology of porous mixtures is strain dependent. The effective viscosity (η_e) of the material during deformation can be modeled as exponentially increasing with decreasing porosity resulting in non-linear ε–t paths.

Acknowledgements

References

Acocella, V., Funiciello, R., Marotta, E., Orsi, G., de Vita, S., 2003. The role of extensional structures on experimental calderas and resurgence. J. Volcanol. Geotherm. Res. 129, 199–217.

Akelaitis, C., 1999. Characterization of Strain during Welding of Pyroclastic Flow Deposits: Devine Canyon, USA and Mt. Meager, Canada. B.Sc. Honours Thesis, University of British Columbia, Vancouver, BC, 31 pp.

Austin, N.J., 2003. An Experimental Investigation of Textural Controls on the Brittle Deformation of Dolomite. Masters thesis. University of British Columbia, 95 pp.

Bansal, N.P., Doremus, R.H., 1986. Handbook of Glass Properties. Academic Press, New York, p. 680.

Bierwirth, P.N., 1982. Experimental Welding of Volcanic Ash. Bachelors Thesis, Monash University.

Boyd, F.R., 1961. Welded tuffs and flows in the rhyolite plateau of Yellowstone Park, Wyoming. Geol. Soc. Am. Bull. 72, 387–426.

Boyd, F.R., Kennedy, G.C., 1951. Some experiments and calculations relating to the origin of welded tuffs. Trans. Am. Geophys. Un. 32, 327–328.

Burcaro, J.A., Dardy, H.D., 1974. High-temperature Brillouin scattering in fused quartz. J. Appl. Phys. 45, 5324–5329.

Dingwell, D.B., Webb, S.L., 1990. Relaxation in silicate melts. Eur. J. Mineral. 2, 427–449.

Ducamp, V.C., Raj, R., 1989. Shear and densification of glass powder compacts. J. Am. Ceram. Soc. 72, 798–804.

Fink, J., Griffiths, R.W., 1990. Radial spreading of viscous gravity currents with solidifying crust. J. Fluid Mech. 221, 485–509.

Friedman, I., Long, W., Smith, R.L., 1963. Viscosity and water content of rhyolite glass. J. Geophys. Res. 68, 6523–6535.

Griffiths, R.W., 2000. The dynamics of lava flows. Annu. Rev. Fluid Mech. 32, 477–518.

Grunder, A.L., Laporte, D., Druitt, T.H., 2005. Experimental and textural investigation of welding: effects of compaction, sintering, and vapor-phase crystallization in the rhyolitic Rattlesnake Tuff. J. Volcanol. Geotherm. Res. 142, 89–104 (this issue).

Guest, J.E., 1967. The sintering of glass and its relationship to welding in ignimbrites. Proc. Geol. Soc. Lond. 1641, 174–177.

Handin, J., Friedman, M., Logan, J.M., Pattison, L.J., Swolfs, H.S., 1972. Experimental folding of rocks under confining pressure; Buckling of single-layer rock beams. Flow and fracture of Rocks. Geophysical Monograph, Am. Geophys. Union, vol. 16, pp. 1–28.

Hill, I.G., Sturtevant, B., 1990. An experimental study of evaporation waves in superheated liquid. In: Meier, G.E.A., Thompson, P.A. (Eds.), Adiabatic waves in liquid–vapor systems. IUTAM Symp. Goettingen, vol. 1989, pp. 25–37.

Lakatos, T., 1976. Viscosity–temperature relations in glass composed of SiO_2–Al_2O_3–Na_2O–K_2O–Li_2O–CaO–MgO–BaO–PbO–B_2O_3. Glastek. Tidskr. 31, 51–54.

Lavallee, Y., Stix, J., Kennedy, B., Richer, M., Longpre, M.-A., 2004. Caldera subsidence in areas of variable topographic relief: results from analogue modelling. J. Volcanol. Geotherm. Res. 129, 219–236.

Mader, H.M., Zhang, Y., Phillips, J.C., Sparks, R.S.J., Sturtevant, B., Stolper, E., 1994. Experimental simulations of explosive degassing of magma. Nature 372, 85–88.

Mangan, M., Mastin, L., Sisson, T., 2003. Gas evolution in eruptive conduits: combining insights from high temperature and pressure decompression experiments with steadystate flow modeling. J. Volcanol. Geotherm. Res. 129, 23–36.

Maxwell, J.C., 1867. On the dynamical theory of gases. Philos. Trans. R. Soc., A 157, 49–88.

Miller, T.F., 1990. A numerical model of volatile behavior in nonwelded cooling pyroclastic deposits. J. Geophys. Res. B 95, 19349–19364.

Mossing, M., 2003. The role of temperature, stress, strain and porosity on pumice from Mount Meager, Canada. B.Sc. Honours Thesis, University of British Columbia, Vancouver, B.C., 25 pp.

Mourtada-Bonnefoi, C.C., Mader, H.M., 2003. Experimental observations of the effect of crystals and pre-existing bubbles on the dynamics and fragmentation of vesiculating flows. J. Volcanol. Geotherm. Res. 129, 83–97.

Peterson, D.W., 1979. Significance of the flattening of pumice fragments in ash-flow tuffs. In: Chapin, C.E., Elston, W.E. (Eds.), Ash-flow tuffs. Spec. Pap. Geol. Soc. Am. 180, 195–204.

Phillips, J.C., Lane, S.J., Lejeune, A.-M., Hilton, M., 1995. Gumrosin-acetone system as an analogue to the degassing behaviour of hydrated magmas. Bull. Volcanol. 57, 263–268.

Quane, S.L., Russell, J.K., 2004. Ranking welding intensity in pyroclastic deposits. Bull. Volcanol. (doi:10.1007/s00445-004-0367-5).

Quane, S.L., Russell, J.K., Kennedy, L.A., 2004. A low-load, high-temperature deformation apparatus for volcanological studies. Am. Mineral. 89, 873–877.

Ragan, D.M., Sheridan, M.F., 1972. Compaction of the Bishop Tuff, California. Geol. Soc. Am. Bull. 83, 95–106.

Riehle, J.R., 1973. Calculated compaction profiles of rhyolitic ash-flow tuffs. Geol. Soc. Am. Bull. 84, 2193–2216.

Riehle, J.R., Miller, T.F., Bailey, R.A., 1995. Cooling, degassing and compaction of rhyolitic ash flow tuffs; a computational model. Bull. Volcanol. 57, 319–336.

Roche, O., Druitt, T.H., Merle, O., 2000. Experimental study of caldera formation. J. Geophys. Res. 105, 395–416.

Ross, C.S., Smith, R.L., 1961. Ash-flow tuffs their origin, geologic relations, and identification. U.S. Geol. Surv. Prof. Pap. 366, 81 pp.

Russell, J.K., Quane, S.L., 2005. Rheology of welding: inversion of field constraints. J. Volcanol. Geotherm. Res. 142, 173–191 (this issue).

Scott, G.D., Kilgour, D.M., 1969. The density of random close packing of spheres. J. Appl. Phys. 2, 863.

Sheridan, M.F., Ragan, D.M., 1976. Compaction of ash flow tuffs. In: Wolf, G.V.C.a.K.H. (Ed.), Developments in Sedimentology. Elsevier, Amsterdam, pp. 677–713.

Smith, R.L., 1960a. Ash flows. Geol. Soc. Am. Bull. 71, 795–842.

Smith, R.L., 1960b. Zones and zonal variations in welded ash flows. U.S. Geol. Surv. Prof. Pap. 354-F, 149–159.

Smith, R.L., Bailey, R.A., 1966. The Bandelier Tuff; a study of ash-flow eruption cycles from zoned magma chambers. Bull. Volcanol. 29, 83–103.

Smith, R.L., Friedman, I.I., Long, W.D., 1958. Welded tuffs, Expt. 1. Trans. Am. Geophys. Union 39, 532–533.

Soule, S.A., Cashman, K.V., 2003. The mechanical properties of solidified polyethylene glycol 600, an analog for lava crust. J. Volcanol. Geotherm. Res. 129, 139–153.

Sparks, R.S.J., Wright, J.V., 1979. Welded air-fall tuffs. In: Chapin, C.E., Elston, W.E. (Eds.), Ash-flow tuffs. Spec. Pap. Geol. Soc. Am. 180, 155–166.

Sparks, R.S.J., Tait, S.R., Yanev, Y., 1999. Dense welding caused by volatile resorption. J. Geol. Soc. (Lond.) 156, 217–225.

Spieler, O., Dingwell, D.B., Alidibirov, M., 2003. Magma fragmentation. J. Volcanol. Geotherm. Res. 129, 109–123.

Streck, M.J., Grunder, A.L., 1995. Crystallization and welding variations in a widespread ignimbrite sheet; the Rattlesnake Tuff, eastern Oregon, USA. Bull. Volcanol. 57, 151–169.

Sura, V., Panda, P., 1990. Viscosity of porous glasses. J. Am. Ceram. Soc. 73, 2697–2701.

Taneda, S., 1957. Geological and petrological studies of the "Shirasu" in south Kyushu, Japan; part II, Preliminary note (2). Mem. Fac. Sci., Kyushu Univ., Ser. D, Geol. 6 (2), 91–105.

Wolff, J.A., Wright, J.V., 1981. Rheomorphism of welded tuffs. J. Volcanol. Geotherm. Res. 10, 13–34.

Yagi, K., 1966. Experimental study on pumice and obsidian. Bull. Volcanol. 29, 559–572.